Iceberg Detection in Dual-Polarized C-Band SAR Imagery by Segmentation and Nonparametric CFAR (SnP-CFAR)

Juha Karvonen, *Member, IEEE*, Alexandru Gegiuc, Tuomas Niskanen, Anni Montonen, Jørgen Buus-Hinkler, and Eero Rinne

***Abstract*— We propose an unsupervised method for iceberg detection over sea ice-free waters. The algorithm is based on the segmentation and nonparametric constant false alarm rate (SnP-CFAR) approach. Unlike in parametric CFAR detection, in our method, there is no need to define target, guard, and background areas explicitly. Instead, we apply the CFAR detection to the pixels within each detected segment and the background is formed of the nearby pixels not included in the target segment. By using nonparametric background probability density function (PDF) estimates, we also eliminate the need of assuming a specific type of a background PDF. We compared the detection results with the operational Danish Meteorological Institute (DMI) Gamma-CFAR algorithm results. The results were evaluated against icebergs manually identified by the Finnish Meteorological Institute (FMI) Ice analysts. Our method also exhibits a reduced number of false alarms. We present results of iceberg detection based on the SAR channel-cross-correlation (CCC). CCC was able to distinguish many of the true targets with a low number of false alarms. However, CCC seems to miss some of the true targets and its main use would be in confirming iceberg observations.**

***Index Terms*— C-band, constant false alarm rate (CFAR), dual-polarized, iceberg detection, SAR, segmentation and nonparametric constant false alarm rate (SnP-CFAR).**

I. Introduction

DURING summer, ice-covered seas in the Arctic region are gradually opening, freeing trapped Icebergs, and ice floes into the open sea. New icebergs are calved from active glaciers. For example, Greenland glaciers reach up to 30 000 calvings per year [1]. Icebergs pose a significant risk to navigation and off-shore activities, if not detected in time. Especially, small icebergs, which can easily be neglected by radar in rough sea surface conditions, can be dangerous. Reliable iceberg monitoring is, therefore, necessary for safe navigation and other marine operations in the areas where icebergs occur.

Targets in open water, including icebergs, typically appear as brighter blocks or dots with respect to their background in SAR imagery, and the most popular method for iceberg detection is thresholding of the SAR backscattering coefficient, σ^0, e.g., in [2]. Some methods also use SAR texture features or other derived quantities to enhance the contrast between the targets and their background. For iceberg detection in open water, similar approaches as for ship detection, e.g., in [3] can be used. In the following, we also provide a short overview of target detection in SAR imagery.

Typical constant false alarm rate (CFAR) methods have some disadvantages. First, they use a fixed pattern for the division to the target area and background area. The target area is the area representing the target (iceberg in this case), and the background area is the area used for estimating the background probability density distribution (PDF) used to define the CFAR threshold. Another typical assumption in CFAR is to use a certain fixed type of parametric PDF, such as the Gamma PDF or the Gaussian PDF. This model may not correspond to the actual local PDF of the SAR data. The third problem is that to detect as much true targets as possible also the number of false alarms may increase to a too high level. To address these shortcomings, we apply SAR segmentation, nonparametric PDF, and channel-cross-correlation (CCC). The segmentation is applied before the CFAR to extract segments that represent either candidate targets or background. This approach makes it possible to use the division of the segments into these two classes, i.e., to define the target and background areas individually for each target candidate. The target candidate pixels are not included in the background area. In the fixed target and background area setup, nearby target pixels could be included in the background. The nonparametric PDF estimation directly uses the background area data to produce the PDF estimate instead of trying to estimate parameters of a certain predefined PDF model. We also studied the use of CCC instead of SAR backscattering in CFAR to reduce the number of false alarms in the iceberg detection. In addition, we have studied the capability of features computed for the targets to distinguish between the true and false targets.

Manuscript received June 2, 2020; revised October 1, 2020, February 13, 2021, and March 26, 2021; accepted March 28, 2021. Date of publication April 16, 2021; date of current version December 20, 2021. This work was supported in part by Vessel Operations and Routing in Ice Conditions (VORIC), a TEKES funded research project, under Contract 40366/14, in part by the European Space Agency (ESA), and in part by the European Commission (EC) Copernicus Marine Environment Monitoring Service (CMEMS) for providing Sentinel-1 SAR data. *(Corresponding author: Juha Karvonen.)*

Juha Karvonen, Tuomas Niskanen, Anni Montonen, and Eero Rinne are with Ilmatieteen Laitos, FI-00101 Helsinki, Finland (e-mail: juha.karvonen@fmi.fi).

Alexandru Gegiuc is with the Finnish Meteorological Institute, FI-00101 Helsinki, Finland.

Jørgen Buus-Hinkler is with the Danmarks Meteorologiske Institut, 2100 Copenhagen, Denmark (e-mail: jbh@dmi.dk).

Digital Object Identifier 10.1109/TGRS.2021.3070312

A. Overview of CFAR Methods for Iceberg Detection

CFAR methods for target detection typically assume a certain parameterized distribution, which can be, e.g., the Gaussian, Gamma, Weibull, or K-distribution. The K-distribution approach is based on the assumption that the backscattering coefficient is Gamma-distributed and that speckle and radar intensity show variations in different scales and can thus be treated separately [4]. K-distribution has been assumed, e.g., in [5] for iceberg detection and in [6]–[8] for ship detection. A theoretical tutorial on the K-distribution in CFAR can be found in [7]. Target detection based on CFAR, K-distribution, and postprocessing by morphological operations was proposed in [9]. The K-distribution and Gamma distribution used for CFAR ship detection were applied in [10]. The distribution model was selected based on the best statistical fit of the distribution to each case. Icebergs within sea ice can also in most cases be detected using a CFAR algorithm. This has been evaluated for C-band single-channel (HH) SAR data in [11].

Iceberg detection based on segmentation has been already demonstrated. In a recent publication [12], segmentation and thresholding with a slightly different approach than the method proposed here have been used in iceberg detection from ENVISAT ASAR wide swath mode (WSM) imagery. Segmentation and thresholding to detect icebergs was also used in [13]. Watershed segmentation and segment features (σ^0 and three shape features) were used for iceberg detection in [14]. A CFAR approach can also be applied after segmentation [15], which will yield more reliable estimates for the background PDF if the estimates are computed within segments and not over segment boundaries. Superpixel oversegmentation technique [16] for ship target detection has been applied in [17] and [18]. This corresponds to our idea of utilizing segmentation to distinguish between the target and CFAR background area automatically for each target candidate without any parameters for target, guard, and background areas. Oversegmentation does not typically split the small target segments but only the background becomes oversegmented, making the oversegmentation approach well suitable for target detection, including iceberg detection.

Gamma distribution CFAR algorithm for iceberg detection has been applied in [19]. This was updated in [20] to become the Danish Meteorological Institute (DMI) operational algorithm, which is part of the Copernicus Marine Environment Monitoring Service (CMEMS) providing open access to Earth observation (EO) and modeled products for registered users. The Gamma distribution CFAR target detection was also studied in [21]. Target (ship) detection using the (generalized) Gamma distribution CFAR was studied in [22]. In [11], a Gaussian distribution was assumed, and the Weibull distribution CFAR ship detection was studied, e.g., in [23] and [24]. Here, we propose to use a nonparametric PDF estimate instead of a parametric distribution. The parametric distribution model would require an assumption of the distribution type, such as the Gaussian or Gamma distribution.

Polarimetric parameters of fully polarimetric SAR data have been studied for iceberg detection and classification, e.g., in [25] and [26]. The 2-D convolution between different polarization channels of polarimetric SAR data improves the contrast between background and ships. This property for ship detection has been utilized in [27]. The possibilities of polarimetry for iceberg detection were studied in [28]. One of the conclusions of [28] was that the cross-polarization ratio is expected to be higher for icebergs than for the background of thin ice or open water and this ratio can be utilized for iceberg detection using dual-polarized SAR imagery. An improved method to increase the contrast between icebergs and the surrounding sea ice or open water for dual-polarized SAR data was proposed in [29]. Their method is called the intensity dual-polarization ratio anomaly detector (iDPolRAD). iDPolRAD has been applied for small iceberg detection in fast ice in [30]. In addition, blob detection was applied to test for the potential CFAR candidates. SAR texture features can also be applied to iceberg detection, e.g., in [32] power-to-mean ratio for iceberg detection has been applied.

Recently, a study [31] used a similar methodology to that we propose here. In their study, segmentation and fully polarimetric SAR data and shape features were used for iceberg detection. Nonsurprisingly polarimetric data gave better results than single- or dual-polarization data. Unfortunately, fully polarimetric data are not yet available in a WSM suitable for large-scale operational monitoring.

Ship detection based on a wavelet transform, the product of the wavelet subbands (to reduce speckle), and a significant factor (a parameter describing the contrast between ships and background) was studied in [33]. The significant factors for the ships in the wavelet subband product grid were significantly higher for the transformed image than for the original image, enabling more reliable thresholding. The assumption behind this was that the statistics of ship response differ from the speckle statistics.

An Alpha-stable distribution CFAR for ship detection was applied by Wang *et al.* [34]. Alpha-stable distributions are derived from the generalized central limit theorem, and, e.g., the Gaussian distribution is a special case of an Alpha-stable distribution. An Alpha-stable distribution is dependent on four parameters. Suitable filtering of the classification result or SAR data can also improve the recognition results. This has been demonstrated, e.g., in [5] and [35].

It is very likely that ships will be recognized as icebergs. In some cases, moving ships can be distinguished based on their wake visible in SAR [36]. For identifying large ships and excluding them from iceberg detection, automatic identification system (AIS) ship identification information [37] can be used.

During recent years, convolutional neural networks (CNNs) [38] have gained popularity in image processing, also in target detection and iceberg, and ship classification. Examples of published ship detection and classification using CNN's are [39]–[41]. Especially, the Statoil/C-CORE Iceberg Classifier Challenge held on Kaggle in 2018 has inspired to search for novel solutions utilizing CNN's in ship and iceberg detection and classification, such as presented in [42]–[45]. CNNs seem to be a very promising approach and will, in the near future, be a considerable alternative to the classical CFAR

algorithms in operational target detection, including iceberg detection.

Above-surface icebergs form a shadow in the range direction and the length of this shadow in SAR range direction is dependent on the incidence angle θ and the above-water height of the iceberg. Assuming a rectangular shape and height h, the shadow size $s = \tan(\theta)$h would be approximately $s = 0.364$ h for an incidence angle of 20° (a typical near range incidence angle value for a ScanSAR SAR image) and $s = 1.192$ h for an incidence angle of 50° (a typical far range incidence angle value). Thus, the shadow sizes are typically too small to be utilized in iceberg detection or classification for ScanSAR medium-resolution imagery. However, shadows may be visible and useful for target detection and classification in high-resolution SAR imagery at the expense narrower swath widths (image size).

During the melt period, many icebergs exhibit a significant decrease in volume scattering due to the wet snow/water layer on top of them [46]. In consequence, the intensity contrast between the target and the background will be very low, and icebergs will not appear as bright targets as during winter. Moreover, if sea clutter, i.e., strong backscatter due to wind-induced sea ice surface roughness (waves), is present, the backscattered radar signal contrast between the targets and background is decreased even more. Naturally, targets in such conditions will most likely be wrongly identified, or not identified at all, by both the automatic and the manual detection. To overcome this problem, we also propose an alternative detection method, which aims to find the targets distinguishable in both the polarization channels, even with a low contrast. For this purpose, we apply the SAR CCC.

B. Practical Implementation of CFAR Algorithms

A CFAR algorithm without segmentation requires definition of the parameters for a sliding window within which the CFAR is performed. The parameters define the radius of the target area, i.e., the area within which the whole target is supposed to be located, and then, typically, a so-called guard area around the target area is used to avoid mixing of the target area with the background area. The sizes of the target, guard, and background areas need to be defined. These areas are shown in Fig. 1 and their sizes are typically defined by the radius R_T for the target area, R_G for the guard area, and R_B for the background area; these values also represent distances from the window center. Their shape typically is a square (corresponding to city block distance) or a circle (Euclidean distance).

From the background distribution, the theoretical threshold corresponding to a given false alarm ratio (FAR) can then be defined. The FAR for a threshold T is

$$\text{FAR} = p(x \geq T) = \int_T^{\infty} P(x)dx = 1 - F(x) \tag{1}$$

where $P(x)$ is the PDF of the background. The cumulative distribution function F(x) is

$$F(x) = \int_{-\infty}^{T} P(x)dx = \frac{\Gamma(\beta, x/\alpha)}{\Gamma(\beta)} \tag{2}$$

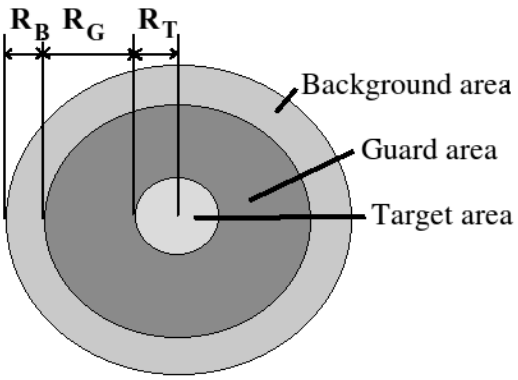

Fig. 1. Schematic of the target, guard, and background areas used in the traditional CFAR approach. R_B, R_G, and R_T are the radiuses of the areas.

where β is the shape parameter, α is the scale parameter of the Gamma function $\Gamma(\beta)$, and $\Gamma(\beta, x/\alpha)$ is the incomplete gamma function. Based on the above relationship, T can numerically be defined for a CFAR. A typical approach is to define the distribution and T locally because the background varies depending on the incidence angle and wave characteristics (wave spectrum). For example, for the Gamma distribution and threshold value T

$$\text{FAR} = \frac{\Gamma(L, T)}{\Gamma(L)} \tag{3}$$

where L is the number of (equivalent) looks, if the distribution parameters have been estimated in a background window of X pixels (depending on R_B and R_G), then $L = XL_e$, where L_e is either the computed number of looks or number of looks given by the products metadata. $\Gamma(L, T)$ is the incomplete gamma function (with integration starting from T instead of zero). From this, T for a given CFAR can be solved numerically.

Here, we propose an algorithm, called segmentation and nonparametric constant false alarm rate (SnP-CFAR), for detecting medium to large (length $\geq$ 60 m) icebergs in sea ice-free water areas based on the SnP-CFAR approach. We concentrate on iceberg detection in open water. However, a similar algorithm could also be adapted for iceberg detection within sea ice. Major advantages of SnP-CFAR are the absence of definition of the typical CFAR parameters: target, guard, and background areas, and the type or family of PDF's used in the CFAR. For a nonparametric distribution used here, the threshold is defined based on the estimated cumulative PDF directly for each target candidate segment background and no explicit formula for it can be given.

II. Data

To test our SnP-CFAR algorithm, we selected a set of 14 Sentinel-1A SAR Extra Wide swath (EW) Ground Range Detected Medium (GRDM) Resolution mode images over waters west and northwest off Greenland acquired in July 2015. Based on visual inspection, these images contained a large number of icebergs.

The wind conditions during our study period varied from calm to windy corresponding to smooth and rough sea surface with different wave spectra producing a wide range of different

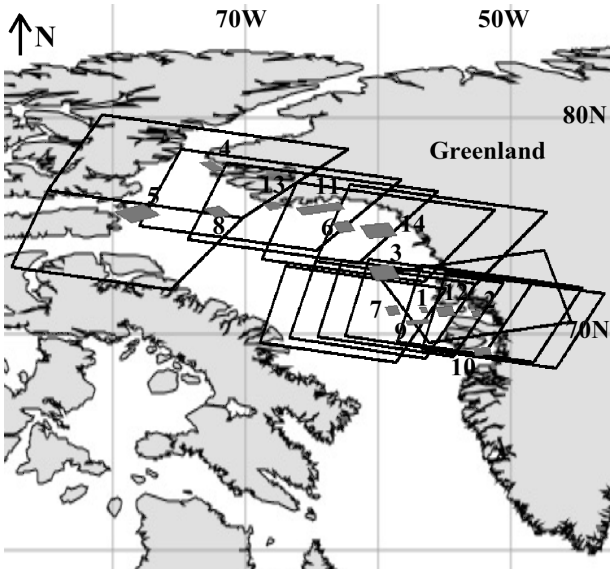

Fig. 2. Sentinel-1A SAR frames (with black boundaries) and data windows (small numbered gray blocks) used in the study drawn over the map of the area. The numbers also refer to the image numbers in Table I. There was one data window corresponding to each SAR image.

TABLE I
SENTINEL-1A SAR DATA SET AND THEIR CORRESPONDING LATITUDE–LONGITUDE CENTER COORDINATES

Image #	Acq. date and time	lat	lon	pass	orbit #
1	2015-07-09 10:56:46	71.07	56.58	A	006733
2	2015-07-09 20:39:09	70.90	52.61	A	006739
3	2015-07-11 10:40:15	72.79	59.57	D	006762
4	2015-07-11 12:17:05	77.71	72.49	A	006763
5	2015-07-11 12:18:05	75.52	78.13	A	006763
6	2015-07-16 10:47:30	74.91	62.58	D	006835
7	2015-07-16 10:48:30	71.02	58.91	D	006835
8	2015-07-17 11:28:21	75.61	72.09	A	006850
9	2015-07-18 10:32:01	70.49	57.04	D	006864
10	2015-07-20 10:15:38	69.15	52.17	D	006893
11	2015-07-26 11:03:56	75.74	64.35	D	006981
12	2015-07-27 10:07:30	71.01	54.92	D	006995
13	2015-07-27 11:44:38	75.86	67.96	A	006996
14	2015-07-28 10:47:30	74.74	59.96	D	007010

SAR backscatters from the sea surface. The data set can be considered representative with respect to weather conditions in Greenland waters. Sea ice was also present in several images. The dual-polarized SAR data (with HH and HV polarization combinations) were resampled to a pixel size of 50 m.

Due to the large spatial coverage of EW mode SAR images (swath width >= 400 km) and our limited resources available for the manual identification of targets for validation, the images were subsetted into smaller regions corresponding to interesting sea ice-free and low sea ice concentration (SIC) areas where the targets could more reliably be distinguished by the ice analysts. Fig. 2 shows the locations of the SAR frames and selected subregions (data windows) used in this study.

Table I contains a list of the used SAR frames with date, time, and central latitude/longitude, including the satellite pass direction (A = Ascending or D = Descending orbit) and the orbit number.

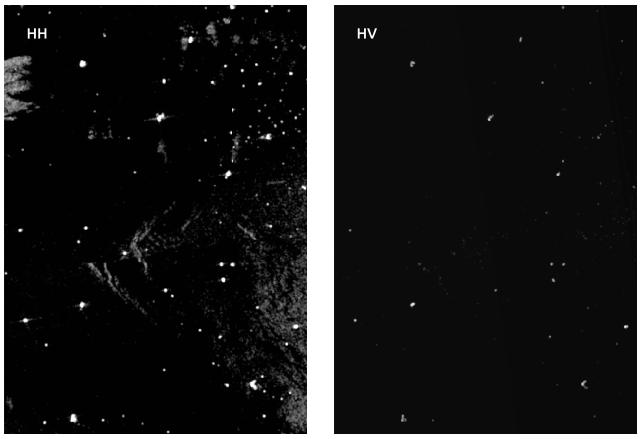

(a) (b)

Fig. 3. Example of Sentinel1A SAR EW GRDM mode image window in (a) HH polarization and (b) HV polarization. Targets can be seen as bright spots in open-water (black) or sea ice areas (gray). This corresponds to the SAR window number 3 in Fig. 2, cropped from the July 11, 2015 10:40:15 UTC image.

To exclude the high SIC areas from the iceberg detection, we have used the daily ARTIST Sea Ice (ASI) algorithm SIC data based on microwave radiometer provided by the University of Hamburg [46] in a 3.125-km grid resolution. We applied the iceberg detection only in the areas of low SIC values with SIC less than 30%. This, however, did not guarantee low SIC. During summer, due to the sensitivity of the AMSR2 passive microwave-based SIC estimation algorithm to surface melt, the amount of sea ice in areas estimated to be <30% by the ASI algorithm can still be significant. Consequently, regions in SAR covered by sea ice or with sea clutter will increase the difficulty of iceberg detection.

Fig. 3 shows an example of an SAR data window used in this study, corresponding to the area number three in Fig. 2 where some sea ice and also sea clutter are present. The gray areas in the right parts of the figure represent both sea ice and sea clutter. Sea clutter and sea ice may be difficult to distinguish if the sea ice consists of small particles. The more compact gray entities in the upper right parts of the figure are ice floes. In the figure, both HH and HV polarization channels are shown. Targets (bright spots) are much easier to find against the dark background than against the brighter sea ice or clutter. There is significantly less clutter and sea ice features visible in the HV than in HH polarization channel.

For performance evaluation purposes, Finnish Meteorological Institute (FMI) Ice Service (FIS) ice analysts were tasked to identify icebergs within our study region and within a time frame defined by the time difference between SAR and optical (i.e., MODIS and Landsat-8) imagery. If a spatial overlap between SAR and optical imagery was found and the temporal difference was no more than two days, optical images were also analyzed. The areas for manual detection were selected so that they included interesting targets and SIC was less than 30%. A total of 2059 manually detected icebergs were used for validating our CFAR method. The recognized icebergs were often close to the shore.

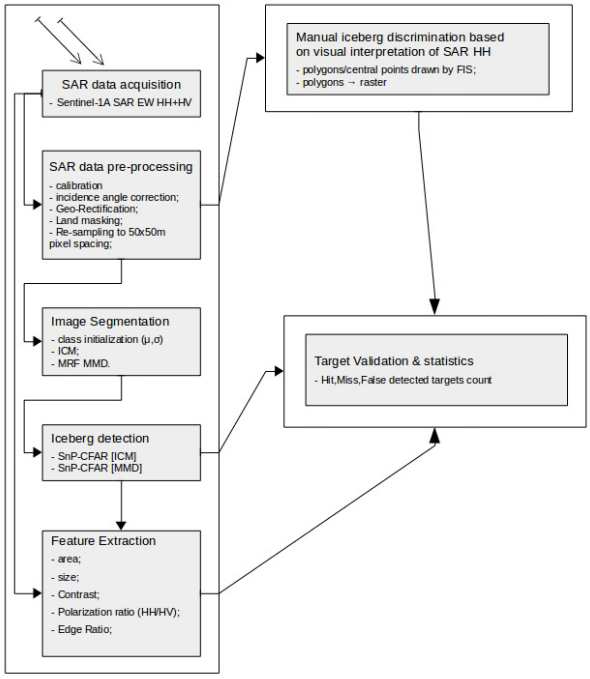

Fig. 4. Block diagram of the iceberg detection algorithm.

Usually, the HH-channel SAR image was clear enough to detect the icebergs but often also HV polarization data provided complementary information for the analysis. Composite images combining SAR HH and HV channels into a single image were successfully used in visual detection. In the composite imagery, the benefits of both HH and HV could be seen at the same time without switching between the images. In most cases, the icebergs recognized in the optical images could also easily be detected in the SAR imagery. Only in few cases, icebergs were detected in the SAR imagery alone.

III. Methodology

A schematic flow diagram of the SnP-CFAR method is presented in Fig. 4. The algorithm is explained in detail in the following sections.

A. SAR Data Processing

For each SAR frame, the backscattering coefficient σ_0 has been radiometrically calibrated based on the Sentinel-1 Product Specification [47], using the σ_0 calibration lookup table (LUT) values provided with the original Level-1 SAR product. After calibration, an incidence angle correction was applied (for details, see [48]). After the incidence angle correction, the images were Geo-rectified into Polar Stereographic coordinate system using the polar stereographic projection with the following parameters: WGS84 datum, reference latitude of 90°, true scale latitude of 70°, and reference longitude of −45°. The data were resampled into pixel spacing of 50×50 m, which approximately corresponds to the original SAR pixel spacing. We also scaled and quantified the calibrated SAR backscattering coefficients to eight bits per pixel. The quantization is even such that −30 dB corresponds to a pixel value of one and 0 dB to the pixel value of 255, and values less than −30 dB are mapped to one and values above 0 dB are mapped to 255. The pixel value zero is reserved for the background, i.e., for the no-data or land pixels. This is the FMI standard SAR processing for the Arctic waters. The spatial resolution of the Sentinel-1 EW GRDM mode SAR images in azímuth direction is 90.1 m, and in range direction, it varies from 90.9 to 95.1 m, the actual pixel spacing being half of the resolution. Our 50-m pixel spacing (size) approximately corresponds to the original pixel spacing, with only very slight undersampling. On the other hand, oversampling does not have any significant effect on the object detection, whereas interpolation effects may even cause undesired smoothing along the target boundaries.

B. SAR Segmentation

We tested two different segmentation approaches for the iceberg SAR imagery: the iterative conditional modes (ICMs) [50] algorithm and Markov random fields (MRFs) [51]–[53]. Both methods have been successfully used in producing different SAR-derived sea ice products at FMI, but they have not earlier been tested in the context of iceberg detection. For iceberg detection, both the methods gave similar results and neither of the methods clearly outperformed the other, based on visual judgment. We chose the ICM segmentation to be used in this study because it is already in use in the operational FMI SAR processing chain of the Baltic Sea ice service and in CMEMS Baltic Sea sea ice products.

Before segmentation, an initial labeling of the SAR image pixels is performed. Assuming that each whole SAR image σ^0 data has a Gaussian mixture distribution, we perform an initial labeling that uses a maximum number of 30 possible different categories based on a Gaussian decomposition of the distribution of the σ^0 values. The number 30 represents a large enough number of categories to capture all the present ice and open water classes, including possible icebergs. In the beginning, the number of categories is set to a given minimum number of categories (here 20) and the Gaussian decomposition is extracted using the expectation–maximization (EM) algorithm [54]. If the derived Gaussian decomposition corresponds to the normalized image histogram well enough, the number of categories (N_c) is retained and the N_c labels are assigned to the SAR pixels. If the correspondence between the SAR histogram and the decomposition is not good enough, the number of categories is increased iteratively until the correspondence becomes good enough or the maximum number of 30 allowed categories has been reached. After stopping the iteration, the initial categories are assigned to SAR pixels, i.e., labels from one to N_c. Here, the coefficient of determination (R^2) has been used as a measure of the similarity between the normalized σ^0 histogram and the Gaussian mixture defined by the N_c Gaussians corresponding to the pixel categories. A threshold of 0.95 for R^2 was applied here, i.e., the stopping conditions for the iteration were $R^2 > 0.95$ or $N_c >= 30$. After the decomposition, each pixel was

TABLE II
DETECTION PARAMETERS USED BY GAMMA-CFAR (IN PIXELS EXCEPT FOR THE CFAR THRESHOLD)

kernel size	background area	guard area	target area	CFAR threshold
37x37	144	35x35 (1224)	1	10^-7

TABLE III
DETECTION PARAMETERS USED BY SnP-CFAR

R_T	R_G	R	T	wsz	N_{min}	N_{max}	T_s	T_c	p	R_b
1	5	1	10	21	20	30	150	5	0.01	11

initially labeled to belong to the most likely Gaussian of the Gaussian decomposition (i.e., the Bayesian approach). After this initialization, the ICM segmentation algorithm was applied until convergence.

C. Iceberg Detection Algorithm

The first step of the SnP-CFAR algorithm is to locate all the segments that have a higher average σ^0 than their background added by a small threshold value T_c. As the SAR pixels representing the SAR backscattering are scaled into the range 1–255, T_c would also take a numeric value between 1 and 255. Here, we have used the value of $T_c = 5$. The most important criterion for selecting T_c is to select a small enough value to include all the potential iceberg segments. The selected value could be smaller (≥ 1), and then, only more iceberg candidates will be included in the CFAR detection. Experimentally, the value of five, corresponding to 0.59 dB, was found suitable to keep the amount of iceberg candidates reasonable (to exclude most of the obvious speckle-induced small bright spots). To reduce the computation time, an upper bound of segment size T_s was applied to exclude the segments larger than 150 pixels from the computation. Such large targets are too large to be of interest for our algorithm. We did not set a lower bound to the target size.

After the candidate segments have been identified, a nonparametric CFAR is applied to each segment to define whether it is a possible iceberg or not. First, the PDF is estimated from the neighboring pixels of the candidate segment, using a Gaussian kernel, within a fixed radius $R_b = 11$ pixels from the segment boundary. The iceberg candidate segment pixels are excluded from the PDF estimation to ensure the inclusion of only background pixels. This ensures that the PDF is considering the local statistics, which can vary considerably between backgrounds of different targets. The algorithm is not especially sensitive to the selection of R_b, it just needs to be large enough to guarantee enough background samples to be able to reliably estimate the background PDF, and according to our experience, values of $R_b < 5$ may lead to unreliable background PDF estimation in some cases.

The last step is to perform the CFAR thresholding to define whether the target segment will be classified as an iceberg or not. The CFAR threshold used here was defined experimentally based on two data windows that were not included in the test set.

The obvious advantage of the nonparametric CFAR is that we do not need any assumptions of the background distribution, such as the Gaussian, Gamma, or K-distribution, and neither need to define the target and background computation windows for CFAR computations, we only define a large enough computation radius for the background and the pixel included in the target, and the background area is then selected automatically based on the preclassification made by the initial iceberg candidate segment selection.

In the case of the DMI Gamma-CFAR, used as a reference method here, the entire CFAR kernel is a 37×37 window centered on the target or pixel of interest (R_T), with the outer single-pixel edge (144 pixels) of the kernel serving as the background band R_B (144 pixels in total) and the inner 35×35 window serving as the guard band R_G (1224 pixels in total). This corresponds to a square-shaped window model with $R_T = 0.5$, $R_G = 17$, and $R_b = 1$ (see Fig. 1). The parameters used in SnP-CFAR and Gamma-CFAR detection are listed in Tables II and III, respectively.

D. Utilization of Dual-Polarized Data

Dual-polarimetric data were utilized in this study in two ways. The first approach was to perform the iceberg detection for both channels separately. The channelwise binary detection results were then combined by applying the logical OR operator. The second approach to utilize dual-polarized data was first to compute HH and HV CCC, to which the SnP-CFAR algorithm was then applied. This experiment demonstrates the usefulness of the SAR CCC in target detection and its confirmation.

The cross correlation C_c between the two SAR polarization channels (HH and HV) windows, here denoted by Y (HH) and Z (HV), is

$$C_c(k,l) = \frac{1}{N\sigma_y\sigma_z} \times \sum_{i,j\in Y,Z} \big(Y(k+i,l+j)-\mu_y\big)\big(Z(k+i,l+j)-\mu_z\big) \quad (4)$$

where k and l refer to the row and column coordinates of the image pixel, respectively, σ_y and μ_y are the mean and standard deviation, respectively, of the window in Y, and σ_z and μ_z are the mean and standard deviation, respectively, of the window in Y. N is the number of pixels within the window. Spherical windows with a radius of five pixels ($R = 5$) were used here in the computation of C_c. C_c is also quantized to eight bits per pixel such that the value $C_c = 0.0$ corresponds to pixel value of one and the value $C_c = 1.0$ to the value 255. The pixel value of zero is again reserved for the background. The iceberg

detection using the CCC approach is also based on SnP-CFAR. We used the ICM segmentation with the same parameters as in our standard SAR segmentation in the detection based on CCC.

E. Performance Measures

To evaluate the performance of the SnP-CFAR algorithm against the operational DMI algorithm (D), we computed the precision P_m, also known as detection rate, which indicates that the proportion of true targets detected out of all detected. P_m is computed as

$$P_m = \frac{T_P}{N_D} = \frac{T_P}{T_P + F_P} \tag{5}$$

where T_P or true positives is the number of targets detected by the automated methods that are also manually defined as icebergs, F_P or false positives is the number of detected targets that are not manually defined as icebergs, and N_D is the total number of detected targets (i.e., $N_D = T_P + F_P$). Similarly, sensitivity, or recall, performance measure R_m, is calculated as

$$R_m = \frac{T_P}{N_R} = \frac{T_P}{T_P + F_N} \tag{6}$$

where N_R is the number of icebergs according to the reference data (i.e., here a number of targets manually detected) and F_N is the number of false negatives or targets that are not detected by the automated methods but are manually recognized to be icebergs.

A measure describing the overall performance of an algorithm, denoted by G, can then be computed as product between P_m and R_m

$$G = P_m R_m. \tag{7}$$

To see how well SnP-CFAR compares with other CFAR target detectors (ships or icebergs), we computed a quality factor FOM as defined in [55]

$$\text{FOM} = \frac{\text{TP}}{\text{FP} + \text{TP} + \text{FN}}. \tag{8}$$

FOM considers both the detection rate and false alarm rate. A higher value of FOM in general indicates a better detection method.

IV. Experimental Results and Comparison to Manual Iceberg Detection

Here, we provide examples of the iceberg detection and compare the performance of SnP-CFAR and the operational DMI Gamma-CFAR applied to our test data set based on the performance metrics presented in Section III-E. For each detection method, we computed T_P, F_P, and F_N by intersecting all of the detected targets with the true targets N_R from the reference data of manually identified icebergs by FIS ice analysts. These results are based on independent detection of the HH and HV polarization channels that were then combined using the logical OR operator.

Table IV shows the total number of T_P, F_N, and F_P for the three detection methods, with the manually detected icebergs N_R as a reference for the whole SAR data set. The number of T_P targets is in agreement between the Gamma-CFAR and SnP-CFAR, with a total of 1805 and 1739, correctly detected targets. These numbers also follow the human recognition results. The SnP-CFAR (CCC), however, correctly detected only 1361 targets out of 2059, having missed more than a quarter of the true number of targets. At the same time, SnP-CFAR (CCC) shows a lower number of false alarms (i.e., 668) than the Gamma-CFAR (i.e., 750), which means that the method should still be considered as a candidate. In contrast, SnP-CFAR seems to produce a reduced number of false alarms, reduced almost to half when compared with the other two methods.

TABLE IV
ICEBERG DETECTION RESULTS

Method	N_R	TP	FP	FN
Gamma-CFAR		1805	750	254
SnP-CFAR	2059	1739	444	320
SnP-CFAR (CCC)		1361	668	698

On the other hand, F_P targets are not as uniformly distributed between the methods in different images as the T_P targets, showing strong differences for some images (e.g., in image 5, $\text{FP}_{\text{Gamma-CFAR}}$ is the highest and $\text{FP}_{\text{SnP-CFAR}}$ is the lowest; in image 10, $\text{FP}_{\text{Gamma-CFAR}}$ is the lowest and $\text{FP}_{\text{SnP-CFAR(CCC)}}$ is the highest.

There are cases when the number of false alarms is up to two or three times the number of the true targets (e.g., image window 10). Some of these targets counted as false alarms can in reality be true targets having a low contrast with respect to the background and could not be recognized visually by the ice analysts. It is possible that if a target is detected in both polarization channels by CCC, then in reality, the target is likely to be a true one. Unfortunately, without additional ground-truth data, we cannot confirm this. Nonetheless, the reader is reminded that visual inspection does not recognize all of the icebergs in the area.

In Fig. 5, we show an example of icebergs detected within an SAR window, in HH and HV polarization channels and the corresponding CFAR detection results by the three methods discussed previously. For the SnP-CFAR, we also show an intermediate step, by highlighting the candidate segments selected for detection. Interestingly, the number of candidate segments is much higher than the actual number of targets detected by SnP-CFAR. This can be explained by the low segment mean value threshold (T_c) applied, which has been applied to guarantee the inclusion of all the potential iceberg candidates.

For evaluation, the manually defined targets, which were initially marked with one vector point each, were enlarged by the morphological dilation operation with a 5×5 pixels kernel, to ensure that at least one-pixel point would overlap with the CFAR detected target. For larger targets, a larger dilation window might be needed for the manually detected targets that could otherwise be included in the false alarms count, especially if the target has multiple intensity maxima or it has broken ice floes in its vicinity.

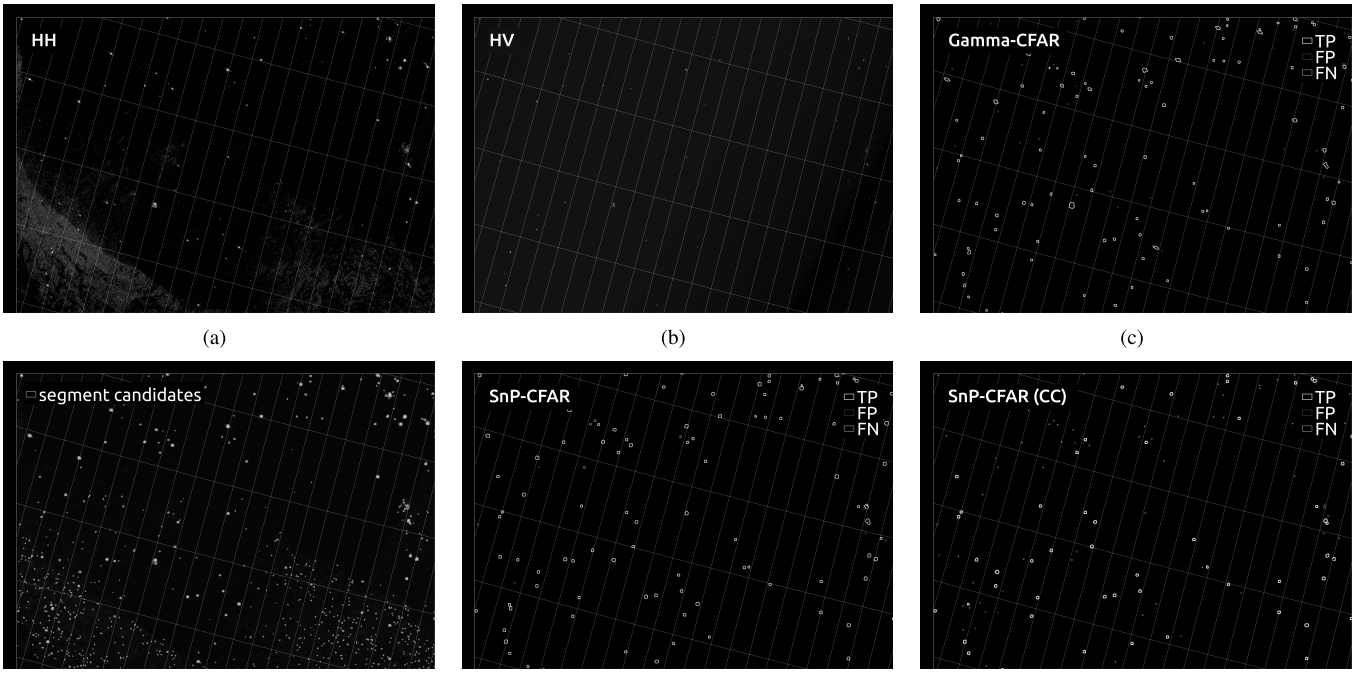

Fig. 5. Example of icebergs seen in an SAR subimage covering both cluttered and clear background. This figure corresponds to the SAR image and window number 10 in Fig. 2 and Table I. (a) Original HH polarization channel SAR image. (b) Original HV polarization channel SAR image. (c) Gamma-CFAR detection results by DMI. (d) Segments mean and the highlighted candidates for detection with CM. (e) SnP-CFAR detection results (TP, FN, and FP) based on (d) SnP-CFAR. (f) SnP-CFAR detection results for the CCC data.

TABLE V
AVERAGE PER IMAGE DETECTION RESULTS

Method	N_R	TP	FP	FN	FOM
Gamma-CFAR		129	54	18	0.65
SnP-CFAR	147	124	32	23	0.72
SnP-CFAR (CCC)		97	48	50	0.52

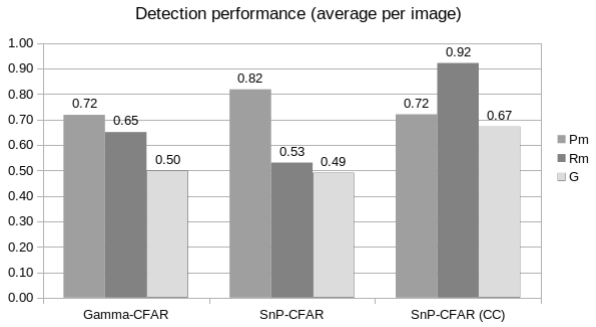

Fig. 6. Iceberg detection performance (average per image) for Gamma-CFAR (DMI), SnP-CFAR based on individual polarization channels, and SnP CFAR (CCC) based on CCC.

Looking at the detection results computed as an average per SAR image (see Table V), we notice that all three detection methods yield similar results. The highest performance with an FOM value of 0.72 is achieved by SnP-CFAR, followed by Gamma-CFAR with FOM of 0.65 and SnP-CFAR (CCC) with FOM of 0.52. This indicates that SnP-CFAR using SAR segmentation as a first step in identifying the possible iceberg candidates and applying the nonparametric CFAR is an improvement over the Gamma-CFAR operational algorithm.

In contrast to FOM, the overall performance results represented by G, which considers the detection precision P_m and its recall R_m, are shown in Fig. 6. The chart shows P_m, R_m, and G for each image with respect to the reference data number of icebergs (N_R).

The best overall score, G, was obtained by CCC SnP-CFAR with 67% detection performance, while the lowest scores of 49% and 50% were obtained by SnP-CFAR and Gamma-CFAR, respectively. The SnP-CFAR again obtained the highest detection rate of 82%, whereas the other two methods scored a detection rate of 72%. The significant difference in performance between the three detection methods is shown by the recall values, with SnP-CFAR (CCC) reaching as high score as 92%, followed by Gamma-CFAR with 65% and finally SnP-CFAR with only 53%.

However, if we look at the P_m and R_m scores independently, the best P_m score was obtained by SnP-CFAR, reaching 82%, followed by Gamma-CFAR and CCC, both with a score of 72%.

The best R_m score was obtained by Gamma-CFAR, reaching 91%, and the lowest R_m score was again obtained by SnP-CFAR (CCC), with 70%, while SnP-CFAR scores were just two percentage points lower than Gamma-CFAR.

These scores demonstrate the usability of the proposed SnP-CFAR detection with SAR segmentation as a preprocessing step. Moreover, the proposed method seems to have at least a comparable performance with the operational Gamma-CFAR algorithm.

TABLE VI
SEGMENTWISE FEATURES

N	Feature	Symbol	Definition
1	Target area	T_A	Number of pixels belonging to the target.
2	Target length	T_L	The diameter of the target bounding box.
3	Aspect ratio	A_R	$A_R = T_L/W = T_L^2/T_A$, where W is the (estimated) width ($W = A/L$) of the target.
4	HH contrast	HH_c	$\overline{\sigma^o_{HH}}(target)$ - $\overline{\sigma^o_{HH}}(background)$, where $\overline{\sigma^o}$ is the average of the pixel values (i.e. scaled dB values).
5	HV contrast	HV_c	$\overline{\sigma^o_{HV}}(target)$ - $\overline{\sigma^o_{HV}}(background)$, where $\overline{\sigma^o}$ is the average of the pixel values (i.e. scaled dB values).
6	Compactness-A	C_A	Indicates how many percents of the target pixels are within radius R from the center (of mass) of the target. R is defined as a radius of a circle with a similar area as the target i.e. $R = \sqrt{A/\pi}$.
7	Compactness-B	C_B	Indicates how many percents of the target pixels are within radius $2 * R$ from the center (of mass) of the target. R is defined as a radius of a circle with a similar area as the target i.e. $R = \sqrt{A/\pi}$.
8	Edge ratio	E_R	The ratio of number of edge pixels in the target (i.e. number of pixels in whose 8-neighborhood exist pixels belonging to other segments) and the object (segment) area. The value has been scaled (multiplied by 100, i.e. is a percentage): $ER = 100 * Ne/A$.
9	Distance ratio	D_R	The ratio of the maximum distance from the target center (of mass) within the target and R (R defined as in 6 and 7). This ratio has been scaled (multiplied) by 100.
10	SAR polarization ratio	$HHHV_{pol}$	HV/HH

V. DISCUSSION

After the SnP-CFAR target identification, we have located the likely iceberg candidates. For these segments, we computed several SAR features describing their contrast with respect to the background and their size and shape. All the computed features are listed in Table VI.

The possibility to further improve the detection based on segment properties was visually evaluated by plotting one feature against another. Of all the computed and studied features, only the contrast and polarization ratio showed discrimination capability between the correctly detected TP, missed FN, and falsely detected FP targets. Other computed features can possibly be used for classification of the targets (e.g., iceberg type, discriminating ships, and icebergs). Fig. 7 shows the scatter plot of the contrast in HH versus polarization ratio for the TP, FN, and FP targets by the SnP-CFAR, for the whole iceberg detection data set. Fig. 7 supports our assumptions regarding the interpretation of the detection results. Most of the false targets seem to have a contrast below 40, while their polarization ratios can be as high as 60. This would indicate that these targets are more difficult to recognize visually and marked as true targets, due to their low contrast values. Furthermore, most of the FN targets are concentrated in the low contrast (≤ 30) and low polarization ratio (≤ 20) values range. This result is more difficult to explain, but it is likely that the human expertise and the complementary data used in manual recognition (e.g., optical data) could make a difference compared to the automatic detection algorithms.

Actually, also CCC magnitude for each segment could be considered as a segment feature and used to confirm iceberg detection. It can be used either independently as a detector of its own or as a feature of the segments produced by segmenting the SAR backscatter imagery. The optimal utilization of CCC will still require further studying.

If we compare the SnP-CFAR detection performance with the ship detection performance tested in [55], we observe a significant difference between the two results. The FOM score for this ship detection method has a value of 0.91 that is higher than the corresponding SnP-CFAR iceberg detection FOM score. However, the differences in FOM could be due to the different data set, likely acquired in different weather conditions, and also due to the large amount of targets (i.e., 2059) in our data set and the very small amount of targets (62) used in the ship detection experiment. We conclude that it is very difficult to fairly compare different detection methods based on the performance statistics for different data sets.

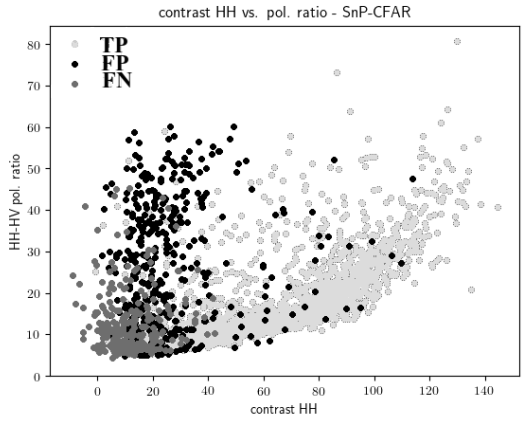

Fig. 7. Contrast (target/background) versus polarization ratio (HH/HV) for the TP, FP, and FN targets detected with SnP-CFAR for the whole data set.

VI. CONCLUSION

In this study, we demonstrated the potential of detecting icebergs in single- or dual-polarized C-band SAR imagery over low SIC or sea ice-free Greenland waters using the SnP-CFAR approach. The performance of our method is comparable with the operational DMI Gamma-CFAR algorithm. In many cases, our method even outperforms the current operational algorithm. Depending on the input data, the segmentation and CFAR threshold parameters may still need fine-tuning for actual operational use.

The SnP-CFAR algorithm uses the ICM image segmentation as a first step in defining the pixel regions with a higher likelihood to contain valid targets based on an experimentally specified segment average σ^0 threshold value. The target detection is then applied to segments using the nonparametric CFAR

approach. This approach can be used for single-polarization channel (HH or HV) or dual polarization by means of SAR CCC, which combines the two channels data into one before applying CFAR. The latter method will only indicate the targets that appear to be highly correlated between the two polarization channels. All of these targets will not necessarily be recognized separately in the HH or HV channels. However, this approach also reduces the likelihood of false alarms. The proposed method showed the best detection FOM score of 72% outperforming the operational Gamma-CFAR algorithm by 7% points.

We believe that our results can be further improved by either improving the quality of the input data by improved preprocessing, such as noise floor correction, scalloping noise removal, and speckle filtering, or fine-tuning our standard segmentation by adjusting its parameters. Parameters could even possibly be adjusted automatically in a data-driven manner. Also, new additional heuristic rules based on intensive data analysis (e.g., different segment mean threshold values for different types of segments) could be developed The SnP-CFAR method could also be further improved, e.g., by utilizing additional information regarding the background statistics of the targets, such as using an adaptive probability threshold value that changes for each target based on the nature of the background distribution. However, such additional development of the algorithm would require a vast data set of SAR data with manually detected icebergs and preferably also spatially and temporally coregistered auxiliary satellite data in high resolution.

One of the advantages of our SnP-CFAR method is also that it is not necessary to define any size restriction to iceberg size: the segments can be small or large assuming that an iceberg is captured as one segment. Naturally, there is a lower limit of a detectable iceberg size due to the used SAR resolution or resampling rate, in this study 50 m. An upper size limit for a target was set here to 150 pixels. It can be set larger if needed. Typically, the icebergs in the Greenland waters are smaller than this threshold. However, for example, in the Antarctic waters, also much larger icebergs can exist.

The DMI Gamma-CFAR algorithm, used as a reference here, has been applied to the original uncalibrated SAR data. These data have a slightly higher resolution than the data produced by the FMI standard processing and may thus improve detection of smaller icebergs in a few cases, but in general, the difference between the original SAR resolution and resolution of our resampled SAR data is not significant for the target detection.

This study was performed using Sentinel-1 SAR data over the Greenland water, but the method can be adapted to any SAR or other EO data over any area where icebergs appear, as the method does not make any assumptions on the signal statistics, more specifically the shape of the PDF.

We also propose a more detailed evaluation of the detection results based on the SAR content for future research. For example, better definition of icebergs is needed in terms of size and SAR backscattering coefficient. Also, the effect of different SAR imagery preprocessing techniques, such as speckle filtering and remapping of the gray tones of the quantized images, could be studied further, even though the use of contextual segmentation already reduces the effect of speckle significantly.

The method at a general level can also be applied to detect icebergs within sea ice using either the SAR backscatter or features derived from the SAR backscatter, e.g., as CCC or backscatter with a contrast enhancement applied. The CFAR threshold naturally needs to be adjusted accordingly. Applying a (CFAR) thresholding to SAR backscattering does not provide good enough iceberg detection results and additional research will be required for developing a reliable operational SAR algorithm to detect icebergs within sea ice.

REFERENCES

[1] D. Diemand, *Icebergs*. Shoreham, VT, USA: Academic, 2001.

[2] C. McCracken, "Techniques for identifying and classifying icebergs in synthetic aperture radar images," Honours Thesis, Dept. Appl. Comput. Math., Univ. Tasmania, Hobart, TAS, Australia, 1995.

[3] D. J. Crisp, "The state-of-the-art in ship detection in synthetic aperture radar imagery, intelligence, surveillance and reconnaissance division information sciences laboratory," Austral. Government Dept. Defence, Defense Sci. Technol. Org., Edinburgh, SA, Australia, Tech. Rep. DSTO-RR-0272, May 2004.

[4] C. J. Oliver and S. Quegan, *Understanding Synthetic Aperture Radar Images*. Boston, MA, USA: Artech House, 1998.

[5] C. Wesche and W. Dierking, "Iceberg signatures and detection in SAR images in two test regions of the weddell sea, Antarctica," *J. Glaciol.*, vol. 58, no. 208, pp. 325–339, 2012.

[6] J. K. E. Tunaley, "Algorithms for ship detection and tracking using satellite imagery," in *Proc. IEEE Int. IEEE Int. IEEE Int. Geosci. Remote Sens. Symp.*, vol. 3, Sep. 2004, pp. 1804–1807.

[7] J. K. E. Tunaley, "K-distribution algorithm, London research and development corporation (LRDC)," London Res. Develop. Corp., Ottawa, ON, Canada, Tech. Rep. LRDC2010-08-10-001, 2010.

[8] J. K. E. Tunaley, "Ship detection in SAR imagery," London Res. Develop. Corp., Ottawa, ON, Canada, Tech. Rep. LRDC2010-12-01-001, 2010.

[9] Y. Ji, J. Zhang, J. Meng, and X. Zhang, "A new CFAR ship target detection method in SAR imagery," *Acta Oceanol. Sin.*, vol. 29, n. 1, pp. 12–16, 2010.

[10] Q. Jiang, S. Wang, D. Ziou, and A. Zaart, "Automatic detection for ship targets in RADARSAT SAR images from coastal regions," in *Proc. Vis. Interface*, Trois-Rivières, Canada, May 1999, pp. 131–137.

[11] K. Lane, D. Power, J. Youden, C. Randell, and D. Flett, "Validation of synthetic aperture radar for iceberg detection in sea ice," in *Proc. IEEE Int. IEEE Int. Geosci. Remote Sens. Symp.*, vol. 1, Sep. 2004, p. 128.

[12] A. K. Mazur, A. K. Wåhlin, and A. Krężel, "An object-based SAR image iceberg detection algorithm applied to the Amundsen Sea," *Remote Sens. Environ.*, vol. 189, pp. 67–83, Feb. 2017.

[13] R. N. Williams, W. G. Rees, and N. W. Young, "A technique for the identification and analysis of icebergs in synthetic aperture radar images of Antarctica," *Int. J. Remote Sens.*, vol. 20, nos. 15–16, pp. 3183–3199, Jan. 1999.

[14] T. A. M. Silva and G. R. Bigg, "Computer-based identification and tracking of Antarctic icebergs in SAR images," *Remote Sens. Environ.*, vol. 94, no. 3, pp. 287–297, Feb. 2005.

[15] P. Lombardo and M. Sciotti, "Segmentation-based technique for ship detection in SAR images," *IEE Proc.-Radar, Sonar Navigat.*, vol. 148, no. 3, pp. 147–159, 2001.

[16] R. Achanta, A. Shaji, K. Smith, A. Lucchi, P. Fua, and S. Süsstrunk, "SLIC superpixels compared to state-of-the-art superpixel methods," *IEEE Trans. Pattern Anal. Mach. Intell.*, vol. 34, no. 11, pp. 2274–2282, Nov. 2012.

[17] T. Li, Z. Liu, R. Xie, and L. Ran, "An improved superpixel-level CFAR detection method for ship targets in high-resolution SAR images," *IEEE J. Sel. Topics Appl. Earth Observ. Remote Sens.*, vol. 11, no. 1, pp. 184–194, Jan. 2018.

[18] O. Pappas, A. Achim, and D. Bull, "Superpixel-level CFAR detectors for ship detection in SAR imagery," *IEEE Geosci. Remote Sens. Lett.*, vol. 15, no. 9, pp. 1397–1401, Sep. 2018.

[19] R. S. Gill, "Operational detection of sea ice edges and icebergs using SAR," *Can. J. Remote Sens.*, vol. 27, n. 5, pp. 411–432, Oct. 2001.

[20] R. Fenger-Nielsen, "Iceberg detection using synthetic aperture radar," M.S. thesis, Fac. Sci., Dept. Geosci. Natural Resour. Manage., Univ. Copenhagen, Copenhagen, Denmark, 2014.
[21] E. Magraner and N. P. Bertaux Réfrégier, "A new CFAR detector in gamma-distributed nonhomogeneous backgrounds," in *Proc. 16th Eur. Signal Process. Conf.*, Lausanne, Switzerland, Aug. 2008, pp. 1–5.
[22] X. Qin, S. Zhou, H. Zou, and G. Gao, "A CFAR detection algorithm for generalized gamma distributed background in high-resolution SAR images," *IEEE Geosci. Remote Sens. Lett.*, vol. 10, no. 4, pp. 806–810, Jul. 2013.
[23] M. Guida, M. Longo, and M. Lops, "Biparametric linear estimation for CFAR against weibull clutter," *IEEE Trans. Aerosp. Electron. Syst.*, vol. 28, no. 1, pp. 138–151, Jan. 1992.
[24] M. Yang, G. Zhang, C. Guo, and M. Sun, "A coarse-to-fine approach for ship detection in sar image based on CFAR algorithm," *Prog. Electromagn. Res. M*, vol. 35, pp. 105–111, 2014.
[25] J. W. Kim, D. S. Kim, H. B. Kim, and J. Hwang, "Iceberg detection using full-polarimetric RADARSAT-2 SAR data in west Antarctica," in *Proc. 3rd Int. Asia–Pacific Conf. Synth. Aperture Radar*, Seoul, South Korea, Sep. 2011, pp. 1–4.
[26] J.-W. Kim, D.-J. Kim, S.-H. Kim, B.-J. Hwang, and J. Yackel, "Detection of icebergs using full-polarimetric RADARSAT-2 SAR data in west Antarctica," *Korean J. Remote Sens.*, vol. 28, no. 1, pp. 21–28, Feb. 2012.
[27] H. Li, Y. He, and W. Wang, "Improving ship detection with polarimetric SAR based on convolution between co-polarization channels," *Sensors*, vol. 9, no. 2, pp. 1221–1236, Feb. 2009.
[28] W. Dierking and C. Wesche, "C-band radar polarimetry—Useful for detection of icebergs in sea ice?" *IEEE Trans. Geosci. Remote Sens.*, vol. 52, no. 1, pp. 25–37, Jan. 2014.
[29] A. Marino, W. Dierking, and C. Wesche, "A depolarization ratio anomaly detector to identify icebergs in sea ice using dual-polarization SAR images," *IEEE Trans. Geosci. Remote Sens.*, vol. 54, no. 9, pp. 5602–5615, Sep. 2016.
[30] I. Soldal, W. Dierking, A. Korosov, and A. Marino, "Automatic detection of small icebergs in fast ice using satellite wide-swath SAR images," *Remote Sens.*, vol. 11, no. 7, p. 806, Apr. 2019.
[31] V. Akbari and C. Brekke, "Iceberg detection in open and ice-infested waters using C-Band polarimetric synthetic aperture radar," *IEEE Trans. Geosci. Remote Sens.*, vol. 56, no. 1, pp. 407–421, Jan. 2018.
[32] R. S. Gill, "Ice cover discrimination in the greenland waters using first-order texture parameters of ERS SAR images," *Int. J. Remote Sens.*, vol. 20, no. 2, pp. 373–385, Jan. 1999.
[33] M. Tello, C. Lopez-Martinez, and J. J. Mallorqui, "A novel algorithm for ship detection in SAR imagery based on the wavelet transform," *IEEE Geosci. Remote Sens. Lett.*, vol. 2, no. 2, pp. 201–205, Apr. 2005.
[34] C. Wang, M. Liao, and X. Li, "Ship detection in SAR image based on the alpha-stable distribution," *Sensors*, vol. 8, no. 8, pp. 4948–4960, Aug. 2008.
[35] C. J. Willis, J. T. Macklin, K. C. Partington, K. A. Teleki, W. G. Rees, and R. G. Williams, "Iceberg detection using ERS-1 synthetic aperture radar," *Int. J. Remote Sens.*, vol. 17, no. 9, pp. 1777–1795, Jun. 1996.
[36] K. Eldhuset, "An automatic ship and ship wake detection system for spaceborne SAR images in coastal regions," *IEEE Trans. Geosci. Remote Sens.*, vol. 34, no. 4, pp. 1010–1019, Jul. 1996.
[37] *IALA Guideline No. 1028 on the Automatic Identification System (AIS) volume 1, Part 1, Operational Issues*, IALA, Saint-Germain-en-Laye, France, Dec. 2004.
[38] Y. LeCun, Y. Bengio, and G. Hinton, "Deep learning," *Nature*, vol. 521, pp. 436–444, May 2015.
[39] C. Bentes, D. Velotto, and B. Tings, "Ship classification in TerraSAR-X images with convolutional neural networks," *IEEE J. Ocean. Eng.*, vol. 43, no. 1, pp. 258–266, Jan. 2018.
[40] P. Vilja, "Vessel detection from SAR images with convolutional neural networks," M.S. thesis, Comput., Commun. Inf. Sci. Programme, Dept. Comput. Sci., Aalto Univ., Espoo, Finland, 2018. [Online]. Available: https://aaltodoc.aalto.fi/handle/123456789/35518
[41] H. Tanveer, T. Balz, and B. Mohamdi, "Using convolutional neural network (CNN) approach for ship detection in Sentinel-1 SAR imagery," in *Proc. 6th Asia–Pacific Conf. Synth. Aperture Radar (APSAR)*, Xiamen, China, Nov. 2019, pp. 1–5.
[42] A. Sagar. (2019). *Deep Learning for Iceberg detection in Satellite Images*. [Online]. Available: https://towardsdatascience.com/deep-learning-for-iceberg-detection-in-satellite-images-c667acf4bad0
[43] C. L. Zhan *et al.*, "Deep learning approach in automatic iceberg—Ship detection with SAR remote sensing data," Cornell Univ., Ithaca, NY, USA, Tech. Rep. 14850, Dec. 2018. [Online]. Available: https://arxiv.org/abs/1812.07367
[44] H. Heiselberg, "Ship-iceberg classification in SAR and multispectral satellite images with neural networks," *Remote Sens.*, vol. 12, no. 15, p. 2353, Jul. 2020.
[45] W. Dai, Y. Mao, R. Yuan, Y. Liu, X. Pu, and C. Li, "A novel detector based on convolution neural networks for multiscale SAR ship detection in complex background," *Sensors*, vol. 20, no. 9, p. 2547, Apr. 2020.
[46] A. Beitsch, L. Kaleschke, and S. Kern, "Investigating high-resolution AMSR2 sea ice concentrations during the february 2013 fracture event in the beaufort sea," *Remote Sens.*, vol. 6, no. 5, pp. 3841–3856, Apr. 2014.
[47] *Sentinel-1 Product Specification*, document S1-RS-MDA-52-7441, European Space Agency, 2016.
[48] J. Karvonen, "Baltic sea ice concentration estimation using SENTINEL-1 SAR and AMSR2 microwave radiometer data," *IEEE Trans. Geosci. Remote Sens.*, vol. 55, no. 5, pp. 2871–2883, May 2017.
[49] *U.S. Geological Survey (USGS) Earth Explorer Web Portal*. Accessed: Apr. 8, 2021. [Online]. Available: https://earthexplorer.usgs.gov/
[50] J. Besag, "On the statistical analysis of dirty pictures," *J. Roy. Statist. Soc., Ser. B*, vol. 48, no. 3, pp. 259–302, 1986.
[51] M. Berthod, Z. Kato, S. Yu, and J. Zerubia, "Bayesian image classification using Markov random fields," *Image Vis. Comput.*, vol. 14, no. 4, pp. 285–295, May 1996.
[52] Z. Kato, "Multi-scale Markovian modelisation in computer vision with applications to spot image segmentation," Ph.D. dissertation, INRIA, Nat. Inst. Res. Digit. Sci. Technol., Sophia Antipolis, France, 1994.
[53] Z. Kato and J. M. Zerubia Berthod, "Satellite image classification using a modified Metropolis dynamics," *Proc. IEEE Int. Conf. Acoust., Speech, Signal Process. (ICASSP)*, San Francisco, CA, USA, vol. 3, Mar. 1992, pp. 573–576.
[54] A. P. Dempster, N. M. Laird, and D. B. Rubin, "Maximum likelihood from incomplete data via the EM algorithm," *J. Roy. Statist. Soc., B Methodol.*, vol. 39, no. 1, pp. 1–38, 1977.
[55] G. Liu, X. Zhang, and J. Meng, "A small ship target detection method based on polarimetric SAR," *Remote Sens.*, vol. 11, no. 24, p. 2938, Dec. 2019.
[56] *EPSG*. Accessed: Apr. 8, 2021. [Online]. Available: http://www.epsg.org/

Juha Karvonen (Member, IEEE) received the M.Sc. (Tech), Lic. Tech., and Dr.Sc. (Tech) degrees in information and computer sciences and digital signal processing from the Helsinki University of Technology (Aalto University since 2010), Espoo, Finland, in 1991, 1996, and 2006, respectively. His Dr.Sc. thesis was dealing with remote sensing of sea ice by SAR.

He has been working in the field of earth observation and remote sensing since 1997. Before that, he worked in the field of industrial machine vision. He is working as a Senior Research Scientist in the Remote Sensing Research Group and Finnish Ice Service, which are parts of the Finnish Meteorological Institute, developing EO products for winter navigation. His main research interests are digital signal and image processing, SAR and other EO data processing, sea ice, and operational marine services.

Alexandru Gegiuc received the B.Sc. double degree in physics and computer science from Alexandru Ioan Cuza Iasi University, Iasi, Romania, in 2008, and the M.Sc. degree in color science (CIMET), awarded by the three distinguished European Universities, part of the Erasmus Mundus European Programme, as follows: Granada University, Granada, Spain, University Jean Monnet, Saint-Étienne, France, and the University of Eastern Finland, Joensuu, Finland, in 2012.

He is with the Polar and Oceanography and Marine Research Group (POM), FMI, Helsinki, Finland. His research interest is mainly centered on image processing, remote sensing, and human–computer vision. Part of his work includes also the development and/or maintenance of different sea ice operational products/services.

Tuomas Niskanen received the M.Sc. degree in geophysics from the University of Helsinki, Helsinki, Finland, in 2009.

He has been with FMI, Helsinki, since 2007 and is holding a development manager position at Finnish Ice Service. Earlier, he worked as an Ice Specialist at DMI from 2011 to 2013, and from 2017 to 2019, he was on a secondment at the European Maritime Safety Agency (EMSA), where he acted as a Project Officer of the Integrated Maritime Data in the Digitization and Application Development Unit.

Anni Montonen received the M.Sc. degree in geophysics from the University of Helsinki, Helsinki, Finland, in 2013.

She is working as an Oceanographer with the Finnish Meteorological Institute, Helsinki, being involved in the operative ice and oceanographic services.

Jørgen Buus-Hinkler received the Ph.D. degree from the University of Copenhagen, Copenhagen, Denmark, in 2005, focusing on snow-precipitation in Northeast Greenland and its relation to sea-ice distribution gathered from passive microwave imagery.

He has been working as a Research Scientist at the Danish Meteorological Institute, Helsinki, Finland, since 2006, within the fields of remote sensing and geospatial analysis. Part of his present work is the development of operational iceberg products based on target detection in SAR imagery. This work is within the Copernicus Marine Environment Monitoring Service (CMEMS). His main research interests are processing of remotely sensed data and geospatial mapping.

Eero Rinne received the M.Sc. (Tech.) degree in space technology from the Helsinki University of Technology, Helsinki, Finland, in 2005, and the Ph.D. degree in geophysics from the University of Edinburgh, Edinburgh, U.K., in 2011.

He has been leading the Polar Oceanography and Sea Ice Research Group, Finnish Meteorological Institute, Helsinki, since 2013. His scientific career has concentrated on satellite remote sensing of the cryosphere, including terrestrial snow, glaciers, and sea ice.

Dr. Rinne is a member of the Mission Advisory Group for future Copernicus mission CRISTAL.